

Measuring gravitational attraction with a lattice atom interferometer

<https://doi.org/10.1038/s41586-024-07561-3>

Received: 18 October 2023

Accepted: 13 May 2024

Published online: 26 June 2024

 Check for updates

Cristian D. Panda¹✉, Matthew J. Tao¹, Miguel Ceja¹, Justin Khouri², Guglielmo M. Tino^{3,4} & Holger Müller¹✉

Despite being the dominant force of nature on large scales, gravity remains relatively elusive to precision laboratory experiments. Atom interferometers are powerful tools for investigating, for example, Earth's gravity¹, the gravitational constant², deviations from Newtonian gravity^{3–6} and general relativity⁷. However, using atoms in free fall limits measurement time to a few seconds⁸, and much less when measuring interactions with a small source mass^{2,5,6,9}. Recently, interferometers with atoms suspended for 70 s in an optical-lattice mode filtered by an optical cavity have been demonstrated^{10–14}. However, the optical lattice must balance Earth's gravity by applying forces that are a billionfold stronger than the putative signals, so even tiny imperfections may generate complex systematic effects. Thus, lattice interferometers have yet to be used for precision tests of gravity. Here we optimize the gravitational sensitivity of a lattice interferometer and use a system of signal inversions to suppress and quantify systematic effects. We measure the attraction of a miniature source mass to be $a_{\text{mass}} = 33.3 \pm 5.6_{\text{stat}} \pm 2.7_{\text{syst}} \text{ nm s}^{-2}$, consistent with Newtonian gravity, ruling out 'screened fifth force' theories^{3,15,16} over their natural parameter space. The overall accuracy of 6.2 nm s^{-2} surpasses by more than a factor of four the best similar measurements with atoms in free fall^{5,6}. Improved atom cooling and tilt-noise suppression may further increase sensitivity for investigating forces at sub-millimetre ranges^{17,18}, compact gravimetry^{19–22}, measuring the gravitational Aharonov–Bohm effect^{9,23} and the gravitational constant², and testing whether the gravitational field has quantum properties²⁴.

A vast experimental programme has been dedicated to testing gravity, including the search for deviations from Newtonian gravity on various scales. Over the past decade, atom interferometry has emerged as a powerful tool in this effort. Quantum experiments with atoms in high vacuum near a miniature source mass have been particularly sensitive to the ultra-weak-field regime^{3–6}. This regime is relevant to theories such as the chameleon^{25,26} and symmetron^{27,28}, whose fifth force is suppressed ('screened') in high-density environments common to solar-system and terrestrial physics experiments. This mechanism allows for building dark-energy models that avoid existing experimental constraints, although the direct connection between 'screened fifth force' theories and dark energy remains a lively point of discussion. Searches for such 'screened' fields have also been performed with neutron interferometry^{29,30} or mechanical systems^{31–33}.

In this work, we use a lattice atom interferometer to measure the tiny acceleration a_{mass} of atoms caused by their interaction with a miniature source mass. Our measurement improves existing constraints on 'screened fifth forces'^{3–6} by factors of 3–5. Projected increases in sensitivity will allow examination of a broad area of the parameter space. To further demonstrate the power of this new atom interferometry

method for precision tests of gravity, we also constrain a generic 'Yukawa' scalar-mediated force and argue that the projected increase in sensitivity based on planned upgrades could make lattice interferometry competitive with state-of-the-art torsion-balance constraints at the sub-millimetre scale^{34–40}.

Caesium (Cs) atoms are held by the optical lattice near a hollow tungsten cylinder with height and diameter of 25.4 mm (Fig. 1a), which acts as a source mass. Each atom is in a quantum spatial superposition state, with each interferometer arm held at two lattice sites along the interferometer axis z that are separated by distance Δz . The atom interferometer measures the potential energy difference, ΔU , between the two arms.

The interaction acceleration, a_{mass} , is measurable because it contributes a potential difference, ΔU_{mass} , between the interferometer arms. To isolate a_{mass} from the approximately 300 million times larger acceleration owing to Earth's gravity, g , as well as systematic effects, we use two switches. The first switch reverses the direction of a_{mass} by positioning the atomic superposition either above ($\tilde{\mathcal{E}} = +1$) or below ($\tilde{\mathcal{E}} = -1$) the source mass. Also, the source mass can be moved close to ($\tilde{\mathcal{M}} = +1$) or far away from ($\tilde{\mathcal{M}} = 0$) the atoms. Each of these switches not only

¹Department of Physics, University of California, Berkeley, Berkeley, CA, USA. ²Department of Physics and Astronomy, University of Pennsylvania, Philadelphia, PA, USA. ³Dipartimento di Fisica e Astronomia, Università di Firenze, INFN, CNR-INO, Sesto Fiorentino, Italy. ⁴European Laboratory for Non-Linear Spectroscopy (LENS), Sesto Fiorentino, Italy. ✉e-mail: cpanda@berkeley.edu; hm@berkeley.edu

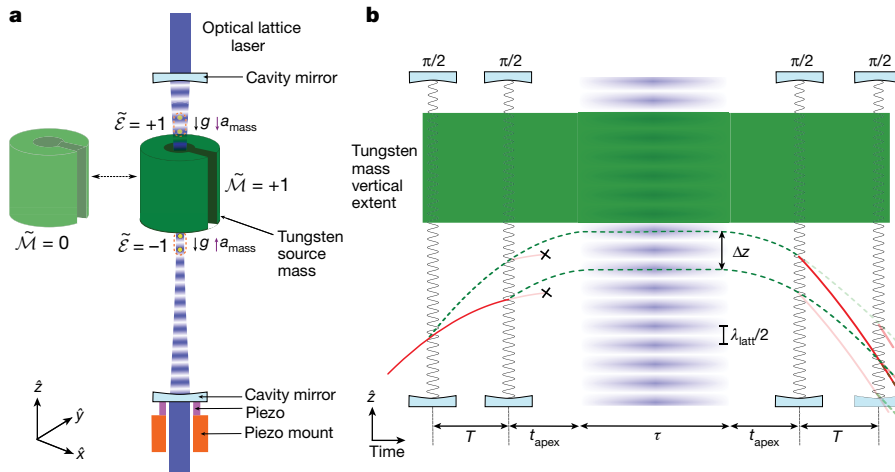


Fig. 1 | Experimental apparatus and lattice atom interferometer trajectories. **a**, A far-detuned, vertical optical lattice (dark blue, wavelength $\lambda_{\text{latt}} = 943 \text{ nm}$) is formed by the mode of an optical cavity established by two mirrors (light blue), which is length-stabilized by a ring piezo (purple). Atoms in a spatial superposition state (yellow circles surrounded by a dashed orange contour) are held in the high-intensity regions of the lattice. They measure the acceleration either above or below the source mass (green). Also, the source mass can be moved near or far from the atoms. A differential measurement

between the $\tilde{\mathcal{E}} \in \{\pm 1\}$ and $\tilde{\mathcal{M}} \in \{+1, 0\}$ configurations yields a_{mass} . **b**, Trajectories of the atoms shown for the $\tilde{\mathcal{E}} = -1, \tilde{\mathcal{M}} = +1$ configuration. The cavity mode (blue stripes) passes through the centre of the tungsten source mass (green). Pairs of $\pi/2$ pulses (wavy vertical lines), separated by time T split, redirect and interfere the atomic wavepackets. At their apex, the wavepackets are loaded into the optical lattice, where they remain for time τ . The internal atomic state is one of the $F = 3$ (solid red lines) or $F = 4$ (dashed green lines) hyperfine levels.

reject the contributions from g and a wide range of systematic errors but also help us characterize systematic effects.

The measured phase shift in state $\tilde{\mathcal{M}} \in \{0, 1\}$, $\tilde{\mathcal{E}} \in \{-1, 1\}$ owing to g and a_{mass} is given by

$$\phi(\tilde{\mathcal{M}}, \tilde{\mathcal{E}}) \approx \Delta U \times \tau / \hbar = m_{\text{Cs}}(g + \tilde{\mathcal{M}}\tilde{\mathcal{E}}a_{\text{mass}})\Delta z \times \tau / \hbar, \quad (1)$$

in which m_{Cs} is the Cs atom mass, \hbar is the reduced Planck constant and τ is the interferometer hold time. The value of a_{mass} is extracted from the change in ϕ that is correlated with the position of the atoms ($\tilde{\mathcal{E}}$) and the position of the source mass ($\tilde{\mathcal{M}}$), that is, with the product $\tilde{\mathcal{M}}\tilde{\mathcal{E}}$. By denoting this correlated component as $\phi^{\mathcal{M}\mathcal{E}}$, we obtain

$$a_{\text{mass}} \equiv a^{\mathcal{M}\mathcal{E}} = \hbar \times \phi^{\mathcal{M}\mathcal{E}} / (\tau \times m_{\text{Cs}} \times \Delta z). \quad (2)$$

Measurement of the interferometer phase

Atoms are prepared in a magneto-optical trap (MOT) with subsequent polarization-gradient cooling and Raman sideband cooling to produce a 300 nK sample of Cs atoms in the magnetically insensitive $m_F = 0$ state of the ground-state hyperfine manifold (see previous paper for details¹⁰). The atoms are launched upwards with a moving optical lattice. A pair of $\pi/2$ Raman pulses (each acting as a 50–50 atomic wavepacket beam splitter), separated by time T , splits the atomic matter wave fourfold (Fig. 1b).

We select two wavepackets that are separated vertically by a distance $\Delta z = 2\nu_r T$, in which $\nu_r = 3.5 \text{ mm s}^{-1}$ is the recoil velocity of Cs atoms from 852 nm photons. These wavepackets share the same internal quantum state and external momentum. When they reach the apex, they are adiabatically loaded into the high-intensity regions of a far-detuned optical lattice (wavelength $\lambda_{\text{latt}} = 943 \text{ nm}$ and trap depth U) with a spatial periodicity $\lambda_{\text{latt}}/2$. The optical lattice beam is mode-filtered by an optical cavity^{11,41–43}. During the hold, the interferometer wavepackets accumulate the relative phase shift, ϕ , owing to potential difference ΔU (equation (1)).

After a hold time τ , the atomic wavepackets are adiabatically unloaded and recombined using a final pair of $\pi/2$ pulses. Their phase difference ϕ determines the probabilities $P_{3,4} = [1 \pm C \cos(\phi)]/2$ that the atoms emerge in either the $F = 3$ or the $F = 4$ state. The fringe contrast C

in the absence of decoherence is $C_0 = 0.5$ because only two of the four interferometer outputs interfere. For detection, we excite the atoms on the Cs D2 line and image the resulting fluorescence signals $S_{3,4}$, which are proportional to $P_{3,4}$. To remove variations in the atom number, both signals are measured simultaneously on the same camera image, using a push beam to spatially separate the $S_{3,4}$ populations (Fig. 2a). From the populations, we then compute the asymmetry,

$$A = (S_3 - S_4) / (S_3 + S_4) = C \cos(\phi). \quad (3)$$

We measure ϕ by recording A while scanning the hold time τ in consecutive iterations (Fig. 2b) and fitting the resulting fringe to a sine wave with the phase ϕ , contrast C and an overall offset as fit parameters.

Sensitivity, data analysis and statistics

Although previous work focused on demonstrating long-lasting coherence¹⁰, here we require high sensitivity to acceleration within a given integration time and therefore a different optimization of the experiment. The theoretical statistical uncertainty at the standard quantum limit (SQL) per experiment shot is given by

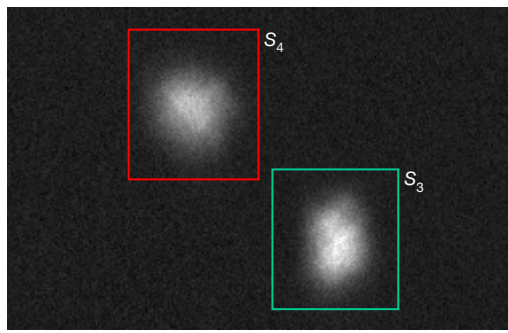
$$\delta a_{\text{shot}}^{\text{SQL}} = \hbar / (m_{\text{Cs}} \times \Delta z \times \tau \times C \sqrt{N_{\text{shot}}}), \quad (4)$$

in which N_{shot} is the number of measured atoms. Also, we empirically determine that contrast decays as $C = C_0 \exp(-\tau \times \Delta z \times U/\kappa)$ (see ref. 10), in which the decay parameter $\kappa = 120 \mu\text{m} \times \text{s} \times E_r$ and $E_r = m_{\text{Cs}}\nu_r^2/2 = \hbar \times 2\pi \times 2.0663 \text{ kHz}$ is the Cs atom recoil energy at 852 nm. The atom number decays as $N = N_0 \exp(-\tau/(12 \text{ s}))$. Given all these constraints, we find that parameters that optimize sensitivity are $\tau = 2.3 \text{ s}$ and $U = 12 E_r$.

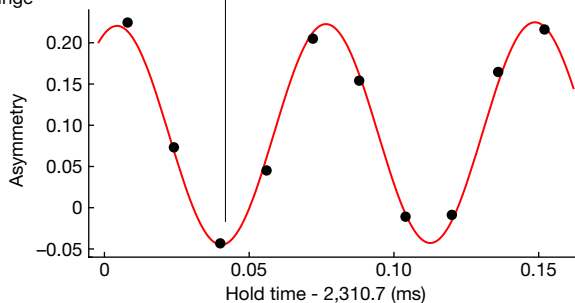
For the fringe shown in Fig. 2b (which is representative of the entire dataset), $C = 0.13$, $\Delta z = 4.2 \mu\text{m}$ and $N_{\text{shot}} \approx 30,000$, and the SQL uncertainty (equation (4)) is $\delta a_{\text{shot}}^{\text{SQL}} \approx 2.2 \times 10^{-6} \text{ m s}^{-2}$. This value is consistent with the measured $\delta a_{\text{shot}} = 2.6 \times 10^{-6} \text{ m s}^{-2}$, showing that the sensitivity of our experiment is consistent with the SQL.

Moreover, δa_{shot} is an order of magnitude smaller than what could have been achieved in previous iterations of the apparatus¹¹, thanks to several improvements, including improved sample preparation, imaging and an efficient moving-lattice launch (described in detail

a Shot image



b Fringe



c Block

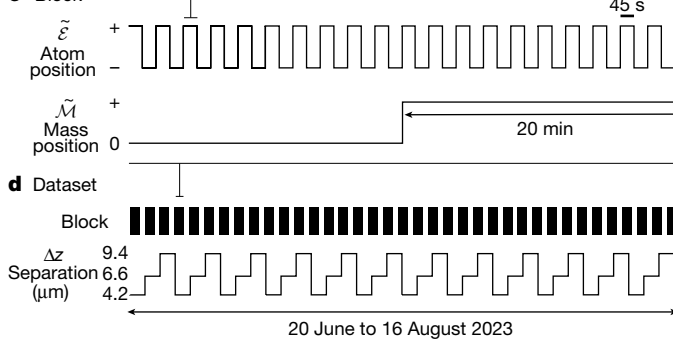


Fig. 2 | Experiment timescales. **a**, Fluorescence image. S_4 and S_3 are the signal intensities summed over the red and green squares. **b**, Measured experimental fringe that typically consists of ten asymmetry points versus hold time τ . **c**, Switches performed within a block. Switch $\tilde{\mathcal{E}}$ alternates from fringe to fringe, whereas switch $\tilde{\mathcal{M}}$ alternates every 20 fringes. **d**, Dataset measuring a_{mass} accumulated over about two months (contains 552 ‘blocks’, not all shown). The interferometer separation, Δz (μm), is varied between three values from block to block, over the entire dataset.

in ref. 10). We also implement an atom elevator based on a far-detuned moving optical lattice (wavelength $\lambda_{\text{latt}} = 943 \text{ nm}$) to shuttle the atoms to various positions along the cavity axis z (such as $\tilde{\mathcal{E}} = \pm 1$).

We switch the atom position ($\tilde{\mathcal{E}}$ switch) from fringe to fringe and the mass position ($\tilde{\mathcal{M}}$ switch) every 20 fringes. This forms a ‘block’ of data, which takes about 40 min to record (Fig. 2c). Each block therefore contains ten measurements of ϕ for each of the 2^2 states corresponding to $\{\tilde{\mathcal{E}}, \tilde{\mathcal{M}}\}$. We average the ten measurements by weighing them by the uncertainty of each measurement.

We then form ‘parity components’^{44,45} of the phase, ϕ^{XY} , which are linear combinations of the measurements that are odd under switch operations X and Y and even under all the other switch operations considered. A superscript ‘nr’ (for non-reversing) denotes a quantity that is even to all switches. In particular, a_{mass} is extracted from ϕ^{ME} , which is odd under the $\tilde{\mathcal{M}}$ and $\tilde{\mathcal{E}}$ switches

$$\phi^{\text{ME}} = [\phi(1, 1) - \phi(1, -1) - \phi(0, 1) + \phi(0, -1)]/2. \quad (5)$$

We then use equation (2) to obtain a_{mass} .

The a_{mass} dataset consists of 552 ‘blocks’ that were taken over a duration of about two months (Fig. 2d). The block dataset time series is shown in Fig. 3a. To test whether a_{mass} depends on wavepacket separation Δz , we also varied between three values $\Delta z = 4.2, 6.6$ and $9.4 \mu\text{m}$ during dataset acquisition. We take approximately equal amounts of data at each separation. τ was not re-optimized because the sensitivity is within 15% of its maximum value for all values of Δz . We find that a_{mass} is independent of Δz (Fig. 3d).

Figure 3b,c shows the statistical distribution of a_{mass} block data, which is consistent with a normal Gaussian distribution. A chi-squared test yields a reduced $\chi_r^2 = 1.06 \pm 0.04$, which we account for by multiplying the statistical uncertainty of the measurement δa^{ME} by $\sqrt{\chi_r^2}$. We observe further excess noise in the channels ϕ^{M} , ϕ^{E} and ϕ^{nr} , which are less protected by the $\tilde{\mathcal{M}}$ and $\tilde{\mathcal{E}}$ switches. This shows that these switches eliminate noise and drift in the experiment.

To prevent experimenter bias, we performed a blind analysis by subtracting an unknown offset from a^{ME} . We revealed this offset only after data collection, statistical data and systematic error analyses were complete.

Systematic errors

As described above, we acquire repeated interferometer measurements under varying experimental conditions to (1) isolate the source-mass acceleration, a^{ME} , from other background noise and errors and (2) search for possible systematic errors. Because a^{ME} is the acceleration component that is correlated with both $\tilde{\mathcal{M}}$ and $\tilde{\mathcal{E}}$ switches, each independently suppresses possible systematic influences of many experimental parameters P on a^{ME} . The uncorrelated parameters, P^{nr} , are suppressed by both switches, whereas parameters correlated with only one switch, P^{M} and P^{E} , are still suppressed by the other switch.

To search for sources of systematic error, we vary experimental parameters P over a larger range than typically found in the experiment and measured their influence on a^{ME} . If P was measured (or is theoretically expected) to have a non-zero influence on a^{ME} , we use further measurements and modelling to determine the systematic dependence of a^{ME} on P , $a^{\text{ME}}(P)$. We use a separated auxiliary measurement to determine the time-averaged ambient value of P , $\langle P \rangle$, and then compute the associated systematic shift, $a_P^{\text{ME}}(\langle P \rangle)$. These data were used only for the determination of systematic shifts and uncertainties and are not included otherwise in the measurement dataset.

Blackbody radiation

The only parameter for which a non-zero shift was either observed or expected is blackbody radiation, which is known in our setup to generate forces on the atoms that are given by $a_{\text{BBR}}^{\text{ME}} = -4.3 \pm 0.6 \times 10^{-8} (T_{\text{mass}}^4 - T_0^4) \text{ nm K}^{-4} \text{s}^{-2}$, in which T_{mass} is the temperature of the source mass and T_0 is the temperature of the environment⁴⁶. We use an infrared thermal sensor to measure T_{mass} and T_0 , which we find to be equal to within $0.05 \pm 0.3 \text{ K}$. We use this measurement to compute a shift and systematic uncertainty that are included in the systematic error budget (Table 1).

Other parameters P are neither observed nor expected to considerably affect a^{ME} , but are nevertheless included in the error budget, as described below.

AC Stark shift difference between atom positions, a^{E}

In the fully retracted position ($\tilde{\mathcal{M}} = 0$), the mass should cause no measurable difference ($< 0.01 \text{ nm s}^{-2}$; see Methods) between the acceleration in the upper ($\tilde{\mathcal{E}} = +1$) and lower ($\tilde{\mathcal{E}} = -1$) positions of the atoms. In the experiment, however, we measure a notable non-zero average a^{E} in the final dataset, $\langle P \rangle = \langle a^{\text{E}} \rangle = -377 \text{ nm s}^{-2}$ with uncertainty $\delta P = 9 \text{ nm s}^{-2}$.

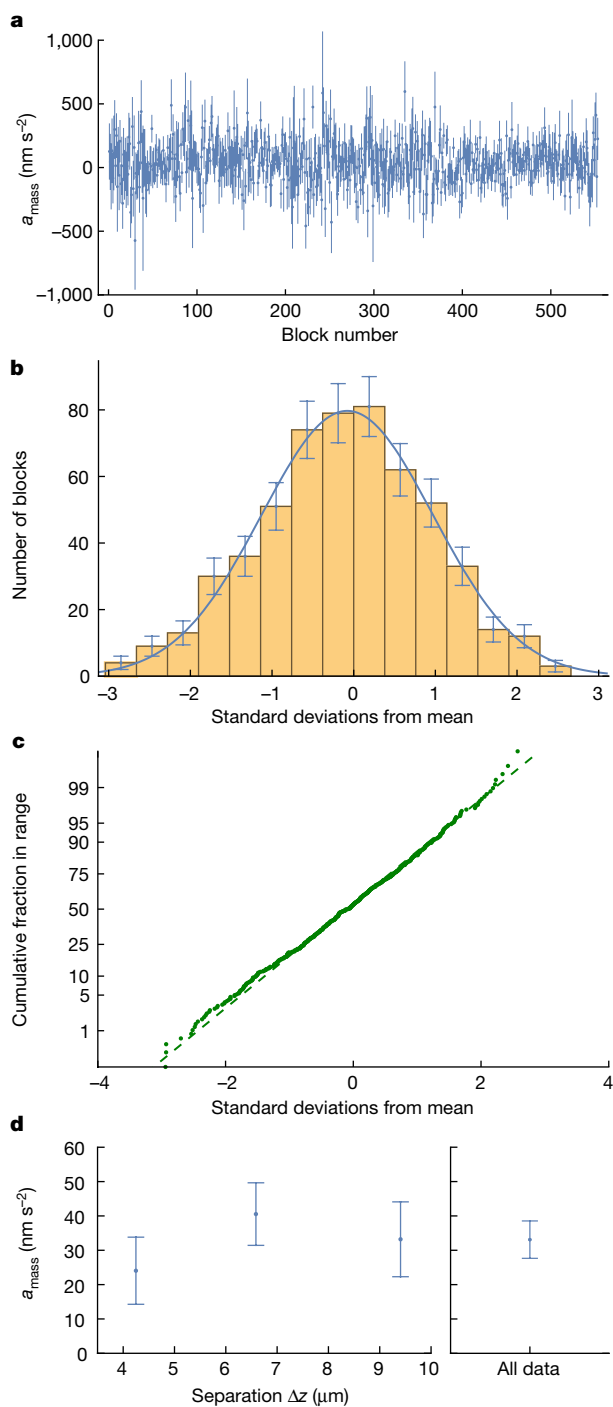


Fig. 3 | Measurement dataset. **a**, Time series of a_{mass} block values. **b**, Histogram of centred and normalized a_{mass} block values. The values are computed from $(a_{\text{mass}} - \langle a_{\text{mass}} \rangle)/\delta a_{\text{mass}}$, in which δa_{mass} refers to the uncertainties of the individual datapoints and $\langle a_{\text{mass}} \rangle$ is the average value over the entire dataset. Error bars indicate the standard deviation in the bin expected from a Poisson distribution. The blue line shows a Gaussian fit to the histogram. **c**, Normal probability plot (green points) compared with a normal distribution (dashed green line). The vertical axis is scaled such that a Gaussian distribution appears linear. **d**, Values of a_{mass} grouped according to separation, Δz , and combined for the entire dataset. Error bars correspond to 1σ (68% confidence interval).

This value is consistent with a model based on the light shift (AC Stark shift) between the two elevator ($\tilde{\varepsilon} = \pm 1$) positions owing to the divergence of the optical lattice mode, as described in detail in Methods.

Table 1 | Systematic shifts and uncertainties in a_{mass}

Parameter	Shift (nms ⁻²)	Uncertainty (nms ⁻²)
Black-body radiation gradient	0.05	1.30
$a^{\mathcal{E}}$ (through $\partial B/\partial z$)		0.07
\mathcal{M} -correlated MOT position		1.86
\mathcal{M} -correlated trap depth		0.31
\mathcal{M} -correlated axial B-field		0.92
\mathcal{M} -correlated transverse B-field		0.84
DC Stark shift		0.50
Total systematic	0.05	2.66
Statistical uncertainty		5.61
Total uncertainty		6.21
Source-mass calculated gravity	35.20	1.00
All uncertainties are added in quadrature.		

Ideally, any effect of $a^{\mathcal{E}}$ on $a^{\mathcal{ME}}$ should be cancelled by the \mathcal{M} (mass position) switch. To quantify the possible residual influence ('leakage') from $a^{\mathcal{E}}$ to $a^{\mathcal{ME}}$, we generate a large artificial $a^{\mathcal{E}}$ by applying a magnetic field gradient, $\partial B_z/\partial z$. We assume a linear relationship between P and $a^{\mathcal{ME}}$ and use these data to determine the slope, $S_p = \partial a^{\mathcal{ME}}/\partial P$, which we measure to be $S_{a^{\mathcal{E}}} = \partial a^{\mathcal{ME}}/\partial a^{\mathcal{E}} = 2.6 \times 10^{-4}$ with an uncertainty δS_p of $\delta S_{a^{\mathcal{E}}} = 1.9 \times 10^{-4}$. Because S_p is consistent with zero, as expected, we apply no systematic correction but use the measured S_p , δS_p , $\langle P \rangle$ and δP to determine the error bar from

$$\delta a_p^{\mathcal{ME}} = \sqrt{(S_p \times \delta P)^2 + (\delta S_p \times \langle P \rangle)^2}. \quad (6)$$

We include this error bar in the systematic error budget (Table 1, entry ' $a^{\mathcal{E}}$ (through $\partial B/\partial z$)').

Contributions owing to $a^{\mathcal{E}}$ - and \mathcal{M} -correlated parameters

Further leakage of $a^{\mathcal{E}}$ into $a^{\mathcal{ME}}$ could result from another parameter that is correlated with the position of the source mass, $P^{\mathcal{M}}$. We identify four such parameters: MOT position, lattice intensity, as well as axial and transverse magnetic fields. We determine the possible systematic error contributions by measuring their associated slopes: $S_{P^{\mathcal{M}}} = \partial a^{\mathcal{ME}}/\partial P^{\mathcal{M}}$, which were all found to be consistent with zero (Extended Data Tables 1 and 2). We use $S_{P^{\mathcal{M}}}$ and $\langle P^{\mathcal{M}} \rangle$ for each of the four parameters to calculate limits that we include in the systematic error budget using equation (6) (Table 1). We discuss each parameter in more detail in the following.

When the mass is inserted ($\mathcal{M} = 0 \rightarrow +1$), we observe a change in the MOT position at the level of 10 μm , which is because of the source-mass mounting rod partially blocking one of the six MOT laser beams. However, we find that the position of the atoms during the measurement is determined by the cavity mode and therefore largely unaffected by the source-mass position. This explains why there is no observed influence of the MOT position on $a^{\mathcal{ME}}$.

Clipping of the cavity laser beam by the source mass is expected to be negligible, as the inner diameter is more than 20 times larger than the radius of the cavity mode. We use the transmission photodetector to observe the intensity of the lattice laser in the $\mathcal{M} = \{0, 1\}$ positions and measure $\langle U^{\mathcal{M}} \rangle$ consistent with zero at the 2 parts in 10^4 level.

Ferromagnetic impurities may give rise to a magnetization of the source mass. We use an auxiliary measurement to determine the residual magnetic field difference between the $\mathcal{M} = \{0, 1\}$ positions, $\langle B^{\mathcal{M}} \rangle$, to be consistent with zero and smaller than 1 mGauss (see ref. 5). We place independent systematic contributions owing to axial (along z) and transverse (along x, y) magnetic fields, as they have different effects on the interferometer phase.

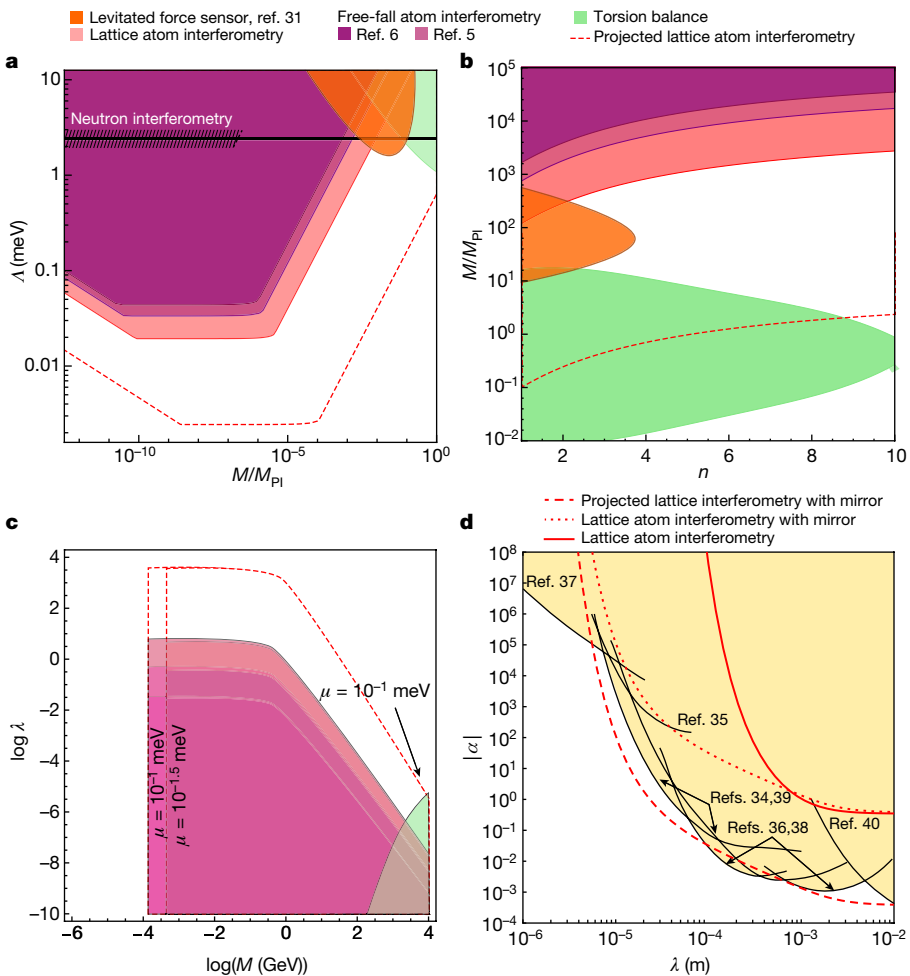


Fig. 4 | Constraints on deviations from Newtonian gravity.

a, Chameleon fields. Shaded areas in the M - Λ parameter plane of a chameleon field are ruled out (see ref. 5 for definitions). $\Lambda \approx 2.4 \text{ meV}$ (black line) is the dark energy level required to drive cosmic acceleration today. Limits from previous experiments are shown: interferometry with atoms in free fall^{5,6}, neutron interferometry^{29,30} and levitated force sensors³¹. **b**, Chameleon limits for $n > 1$. Bounds with $\Lambda \approx 2.4 \text{ meV}$ showing the narrowing gap in which the chameleon gap remains viable. n is the power-law index describing the shape of the chameleon potential. **c**, Symmetron fields. Constraints from atom interferometers and torsion-balance experiments are shown. All shaded areas are ruled out at the 95% confidence level. Projected increases in sensitivity based on planned upgrades in a table-top next-generation apparatus are shown (1,000-fold higher gravitational sensitivity, dashed red line). **d**, Yukawa-type deviation from Newtonian law. Previous experimental bounds^{34–40} are shown as black lines and enclose the excluded region (yellow band). Bounds obtained using the data in this manuscript are shown as a solid red line. The parameter space reach of a new experiment geometry (see text) is shown with current sensitivity (dotted red line) and with projected increases in sensitivity (dashed red line).

Source-mass surface

The source mass is electrically grounded. However, thin films of surface oxidation may form an insulating layer, allowing surface voltages of up to 10 V to form. Using the ground-state polarizability of Cs (ref. 47), even these worst-case scenario voltages would cause a maximum acceleration of only 0.5 nm s^{-2} . We include this contribution in the systematic error budget (Table 1, entry ‘DC Stark shift’). Casimir–Polder effects are negligible⁴⁸, because the atoms never come closer to the source-mass surface than about 4 mm.

As well as the effects above, we varied more than 35 further experimental parameters and measured their effect on a^{ME} (Extended Data Tables 1 and 2). None of these were observed or expected to have an influence on a^{ME} and therefore corresponding error bars were not included in the systematic error budget.

Measured gravitational acceleration and implications

After unblinding, we find $a_{\text{mass}} = 33.3 \pm 5.6_{\text{stat}} \pm 2.7_{\text{syst}} \text{ nm s}^{-2} = 33.3 \pm 6.2 \text{ nm s}^{-2}$ for the acceleration of the atoms towards the source mass. The expected acceleration is $a_{\text{mass}}^{\text{calc}} = 35.2 \pm 1.0 \text{ nm s}^{-2}$ (see Methods). The difference $a_{\text{anomaly}} \equiv a_{\text{mass}} - a_{\text{mass}}^{\text{calc}} = -1.9 \pm 6.3 \text{ nm s}^{-2}$ is consistent with zero. The combined statistical and systematic uncertainty of this measurement has been reduced fourfold from the previous best atom interferometric measurements of the gravity owing to a centimetre-sized source mass^{5,6}. An upper limit $|a_{\text{anomaly}}| < 13 \text{ nm s}^{-2}$ is computed using a folded Gaussian at 95% confidence, which represents a factor of 6 improvement over the previous results achieved with interferometers in which atoms are in free fall^{5,6}.

Our measurement also improves on previous constraints on exotic ‘screened fifth forces’ from chameleon or symmetron particles^{3–6,15,16} by factors of 3–5. Figure 4 shows the excluded parameter ranges for these models. The available parameter space for chameleons with $\Lambda \approx 2.4 \text{ meV}$ (black line), the dark energy level required to drive cosmic acceleration today, is now fully excluded (Fig. 4a). Notable regions of the parameter space with the power index describing the shape of the chameleon potential $n > 1$ have also been constrained (Fig. 4b). Similar improvements are seen for symmetrons (Fig. 4c).

Our measurement also constrains modifications to the Newtonian inverse square law (Fig. 4d, solid red line) that can be parametrized using a ‘generic Yukawa’ scalar-mediated potential $V(r) = -G_N(1 + \alpha e^{-(r/\lambda)}) m_1 m_2 / r$. Also, the dotted red line shows the projected parameter space reached with the same sensitivity but a geometry optimized for testing Yukawa-type forces, in which the atoms are held a distance of 100 μm away from a high-quality cavity mirror that also acts as a source mass, whereas the dashed red line shows the parameter space examined with this geometry and the projected increased sensitivity. The procedure for obtaining these bounds and projections is described in more detail in Methods.

We have demonstrated that interferometry with atoms held in an optical lattice can measure the gravity of a small source mass with an accuracy of 6.2 nm s^{-2} , surpassing interferometry with atoms in free fall in at least this application. Further gains in the sensitivity of lattice-based interferometers could come from increased atom numbers and improved coherence. Empirically and through simulations, we have found that the contrast-decay parameter κ is inversely proportional to atom temperature and the tilt power spectral density¹⁰. Using evaporative cooling may reduce the temperature fivefold⁴⁹ and

active cancellation may reduce the tilt power spectral density about 200-fold at 1 Hz in a table-top setup⁵⁰. This would increase the sensitivity by three orders of magnitude to approximately $5 \text{ nm s}^{-2}/\sqrt{\text{Hz}}$, improving on the best free-fall gravimeters⁵¹. The lattice beam divergence effect described above can be reduced by many orders of magnitude by increasing the diameter of the lattice beam and by holding the atoms near the beam waist, for which divergence is minimized. Long-term stability of the gravimeter at this level could be achieved by tilt stabilization of the cavity axis using piezos. This, along with the relative insensitivity to vibration¹¹ and DC tilt⁵² (as opposed to tilt noise) makes lattice interferometry attractive for inertial sensing^{19,53,54} and mobile gravimetry^{20–22}.

New tests of fundamental physics are also within reach, such as measuring a gravitational phase shift in the absence of forces^{9,23} or signals from non-classical gravity^{17,24}. This increased sensitivity along with the use of kilogram-scale masses, could also enable measurements of G , the gravitational constant², which would benefit from the more precise positioning of the atoms with respect to the source mass enabled by the optical lattice and by holding atoms near source masses smaller than used previously, whose density and volume are easier to characterize. Using schemes that measure G from the phase difference between saddle points of the potential²³, for which the spatial dependence is on the second order (rather than from a potential gradient), would reduce atom positioning errors even further. In the longer term, further sensitivity gains could be achieved with larger-scale upgrades, such as demonstrated vibration isolation in gravitational-wave detectors⁵⁵ and increased atom numbers.

Online content

Any methods, additional references, Nature Portfolio reporting summaries, source data, extended data, supplementary information, acknowledgements, peer review information; details of author contributions and competing interests; and statements of data and code availability are available at <https://doi.org/10.1038/s41586-024-07561-3>.

- Peters, A., Chung, K. Y. & Chu, S. Measurement of gravitational acceleration by dropping atoms. *Nature* **400**, 849–852 (1999).
- Rosi, G., Sorrentino, F., Cacciapuoti, L., Prevedelli, M. & Tino, G. M. Precision measurement of the Newtonian gravitational constant using cold atoms. *Nature* **510**, 518–521 (2014).
- Burrage, C., Copeland, E. J. & Hinds, E. A. Probing dark energy with atom interferometry. *J. Cosmol. Astropart. Phys.* **3**, 042 (2015).
- Hamilton, P. et al. Atom-interferometry constraints on dark energy. *Science* **349**, 849–851 (2015).
- Jaffe, M. et al. Testing sub-gravitational forces on atoms from a miniature in-vacuum source mass. *Nat. Phys.* **13**, 938–942 (2017).
- Sabulsky, D. O. et al. Experiment to detect dark energy forces using atom interferometry. *Phys. Rev. Lett.* **123**, 061102 (2019).
- Asenbaum, P., Overstreet, C., Kim, M., Curti, J. & Kasevich, M. A. Atom-interferometric test of the equivalence principle at the 10^{-12} level. *Phys. Rev. Lett.* **125**, 191101 (2020).
- Dickerson, S. M., Hogan, J. M., Sugarbaker, A., Johnson, D. M. S. & Kasevich, M. A. Multiaxis inertial sensing with long-time point source atom interferometry. *Phys. Rev. Lett.* **111**, 83001 (2013).
- Overstreet, C., Asenbaum, P., Curti, J., Kim, M. & Kasevich, M. A. Observation of a gravitational Aharonov-Bohm effect. *Science* **375**, 226–229 (2022).
- Panda, C. D. et al. Coherence limits in lattice atom interferometry at the one-minute scale. *Nat. Phys.* <https://doi.org/10.1038/s41567-024-02518-9> (2024).
- Xu, V. et al. Probing gravity by holding atoms for 20 seconds. *Science* **366**, 745–749 (2019).
- Zhang, X., del Aguila, R. P., Mazzoni, T., Poli, N. & Tino, G. M. Trapped-atom interferometer with ultracold Sr atoms. *Phys. Rev. A* **94**, 043608 (2016).
- Charrière, R., Cadoret, M., Zahzam, N., Bidel, Y. & Bresson, A. Local gravity measurement with the combination of atom interferometry and Bloch oscillations. *Phys. Rev. A* **85**, 013639 (2012).
- Cladé, P. et al. A promising method for the measurement of the local acceleration of gravity using Bloch oscillations of ultracold atoms in a vertical standing wave. *Europhys. Lett.* **71**, 730–736 (2005).
- Wang, J., Hui, L. & Khoury, J. No-go theorems for generalized chameleon field theories. *Phys. Rev. Lett.* **109**, 241301 (2012).
- Elder, B. et al. Chameleon dark energy and atom interferometry. *Phys. Rev. D* **94**, 044051 (2016).
- Tino, G. M. Testing gravity with cold atom interferometry: results and prospects. *Quantum Sci. Technol.* **6**, 024014 (2021).
- Westphal, T., Hepach, H., Pfaff, J. & Aspelmeyer, M. Measurement of gravitational coupling between millimetre-sized masses. *Nature* **591**, 225–228 (2021).
- Geiger, R., Landragin, A., Merlet, S. & Pereira Dos Santos, F. High-accuracy inertial measurements with cold-atom sensors. *AVS Quantum Sci.* **2**, 024702 (2020).
- Stray, B. et al. Quantum sensing for gravity cartography. *Nature* **602**, 590–594 (2022).
- Janvier, C. et al. Compact differential gravimeter at the quantum projection-noise limit. *Phys. Rev. A* **105**, 022801 (2022).
- Vovrosh, J., Dragomir, A., Stray, B. & Boddice, D. Advances in portable atom interferometry-based gravity sensing. *Sensors* **23**, 7651 (2023).
- Hohensee, M. A., Estey, B., Hamilton, P., Zeilinger, A. & Müller, H. Force-free gravitational redshift: proposed gravitational Aharonov-Bohm experiment. *Phys. Rev. Lett.* **108**, 230404 (2012).
- Carney, D., Müller, H. & Taylor, J. M. Using an atom interferometer to infer gravitational entanglement generation. *PRX Quantum* **2**, 030330 (2021).
- Brax, P., van de Bruck, C., Davis, A. C., Khouri, J. & Weltman, A. Detecting dark energy in orbit: the cosmological chameleon. *Phys. Rev. D* **70**, 123518 (2004).
- Khoury, J. & Weltman, A. Chameleon fields: awaiting surprises for tests of gravity in space. *Phys. Rev. Lett.* **93**, 171104 (2004).
- Olive, K. A. & Pospelov, M. Environmental dependence of masses and coupling constants. *Phys. Rev. D* **77**, 43524 (2008).
- Hinterbichler, K., Khouri, J., Levy, A. & Matas, A. Symmetron cosmology. *Phys. Rev. D* **84**, 103521 (2011).
- Li, K. et al. Neutron limit on the strongly-coupled chameleon field. *Phys. Rev. D* **93**, 062001 (2016).
- Cronenberg, G. et al. A gravity of Earth measurement with a qBOUNCE experiment. In *European Physical Society Conference on High Energy Physics 408* (Proceedings of Science, 2015).
- Yin, P. et al. Experiments with levitated force sensor challenge theories of dark energy. *Nat. Phys.* **18**, 1181–1185 (2022).
- Upadhye, A. Dark energy fifth forces in torsion pendulum experiments. *Phys. Rev. D* **86**, 102003 (2012).
- Betz, J., Manley, J., Wright, E. M., Grin, D. & Singh, S. Searching for chameleon dark energy with mechanical systems. *Phys. Rev. Lett.* **129**, 131302 (2022).
- Kapner, D. J. et al. Tests of the gravitational inverse-square law below the dark-energy length scale. *Phys. Rev. Lett.* **98**, 021101 (2007).
- Geraci, A. A., Smullin, S. J., Weld, D. M., Chiaverini, J. & Kapitulnik, A. Improved constraints on non-Newtonian forces at 10 microns. *Phys. Rev. D* **78**, 022002 (2008).
- Tan, W. H. et al. New test of the gravitational inverse-square law at the submillimeter range with dual modulation and compensation. *Phys. Rev. Lett.* **116**, 131101 (2016).
- Chen, Y. J. et al. Stronger limits on hypothetical Yukawa interactions in the 30–8000 nm range. *Phys. Rev. Lett.* **116**, 221102 (2016).
- Tan, W. H. et al. Improvement for testing the gravitational inverse-square law at the submillimeter range. *Phys. Rev. Lett.* **124**, 051301 (2020).
- Lee, J. G., Adelberger, E. G., Cook, T. S., Fleischer, S. M. & Heckel, B. R. New test of the gravitational $1/r^2$ law at separations down to 52 μm . *Phys. Rev. Lett.* **124**, 101101 (2020).
- Ke, J. et al. Combined test of the gravitational inverse-square law at the centimeter range. *Phys. Rev. Lett.* **126**, 211101 (2021).
- Greve, G. P., Luo, C., Wu, B. & Thompson, J. K. Entanglement-enhanced matter-wave interferometry in a high-finesse cavity. *Nature* **610**, 472–477 (2022).
- Weidner, C. A. & Anderson, D. Z. Experimental demonstration of shaken-lattice interferometry. *Phys. Rev. Lett.* **120**, 263201 (2018).
- McAlpine, K. E., Gochnauer, D. & Gupta, S. Excited-band Bloch oscillations for precision atom interferometry. *Phys. Rev. A* **101**, 023614 (2020).
- Andreev, V. et al. Improved limit on the electric dipole moment of the electron. *Nature* **562**, 355–360 (2018).
- Eckel, S., Hamilton, P., Kirilov, E., Smith, H. W. & DeMille, D. Search for the electron electric dipole moment using Ω -doublet levels in PbO. *Phys. Rev. A* **87**, 052130 (2013).
- Haslinger, P. et al. Attractive force on atoms due to blackbody radiation. *Nat. Phys.* **14**, 257–260 (2018).
- Gregoire, M. D., Hromada, I., Holmgren, W. F., Trubko, R. & Cronin, A. D. Measurements of the ground-state polarizabilities of Cs, Rb, and K using atom interferometry. *Phys. Rev. A* **92**, 052513 (2015).
- Scheel, S. & Buhmann, S. Y. Casimir-Polder forces on moving atoms. *Phys. Rev. A* **80**, 042902 (2009).
- Hung, C. L., Zhang, X., Gemelke, N. & Chin, C. Accelerating evaporative cooling of atoms into Bose-Einstein condensation in optical traps. *Phys. Rev. A* **78**, 011604 (2008).
- Hensley, J. M., Peters, A. & Chu, S. Active low frequency vertical vibration isolation. *Rev. Sci. Instrum.* **70**, 2735–2741 (1999).
- Zhang, T. et al. Ultrahigh-sensitivity Bragg atom gravimeter and its application in testing Lorentz violation. *Phys. Rev. Appl.* **20**, 14067 (2023).
- Panda, C. D., Tao, M., Ceja, M., Reynoso, A. & Müller, H. Atomic gravimeter robust to environmental effects. *Appl. Phys. Lett.* **123**, 064001 (2023).
- Bongs, K. et al. Taking atom interferometric quantum sensors from the laboratory to real-world applications. *Nat. Rev. Phys.* **1**, 731–739 (2019).
- Goossens, S. et al. High-resolution gravity field models from GRAIL data and implications for models of the density structure of the Moon's crust. *J. Geophys. Res. Planets* **125**, e2019JE006086 (2020).
- Maticich, F. et al. Advanced LIGO two-stage twelve-axis vibration isolation and positioning platform. Part 1: design and production overview. *Precis. Eng.* **40**, 273–286 (2015).

Publisher's note Springer Nature remains neutral with regard to jurisdictional claims in published maps and institutional affiliations.

Springer Nature or its licensor (e.g. a society or other partner) holds exclusive rights to this article under a publishing agreement with the author(s) or other rightsholder(s); author self-archiving of the accepted manuscript version of this article is solely governed by the terms of such publishing agreement and applicable law.

© The Author(s), under exclusive licence to Springer Nature Limited 2024

Methods

Determination of source-mass Newtonian gravitational attraction

We use a combination of analytics, finite element analysis modelling and spatial triangulation to determine the expected Newtonian gravitational acceleration from the source mass, $a_{\text{mass}}^{\text{calc}}$.

The tungsten source mass is a hollow cylinder with a height of 25.4 mm, outer diameter of 25.4 mm and inner diameter of 10.0 mm. A rectangular slot with a width of 5.7 mm allows for the insertion and removal of the source mass without blocking the cavity mode. The mass is manufactured using wire electron discharge machining with tolerances better than 10 μm . The calculated source-mass volume is consistent with its measured weight given the density of tungsten to within <1%.

To determine the source-mass position relative to the atoms, we record sequential images of the atom sample and source mass (Extended Data Fig. 1) using three different camera positions. Measuring the position of the atom sample at three different heights along the atomic elevator axis (which coincides with the cavity axis) fully determines (through triangulation) the orientation of the elevator axis with respect to the source mass. This procedure provides a measurement of the two elevator atom positions ($\tilde{\mathcal{E}} = \pm 1$) with respect to the source mass with better than 1 mm accuracy.

To estimate the gravitational acceleration $a_{\text{mass}}^{\text{calc}}$ at this position, we first analytically calculate the gravitational field along the axis of a simple hollow cylinder, disregarding the existence of the slot. We use this calculation to verify the results of a finite element analysis software (COMSOL Multiphysics; because COMSOL does not offer a gravitational module by default, we use the electrostatic module, modifying the ‘charge’ of the source mass to the density of tungsten and using the gravitational constant instead of the electrostatic constant). We find good agreement to better than 0.1%. We then add the rectangular slot to the finite element model to generate a 3D map of the gravitational field (Extended Data Fig. 2).

At the triangulated positions, we find the average source-mass gravitational acceleration along the interferometer axis to equal $a_{\text{mass}}^{\text{calc}} \equiv (a_{\text{mass}}^{\mathcal{E}+} + a_{\text{mass}}^{\mathcal{E}-})/2 = 35.2 \pm 1.0 \text{ nm s}^{-2}$. This uncertainty is dominated by the uncertainty in positioning of the atoms with respect to the source mass. The acceleration in the mass-out position ($\tilde{\mathcal{M}} = 0$) is <0.01 nm s^{-2} and therefore negligible.

Systematic investigation: $a^{\mathcal{E}}$ phase-shift model

We describe here in detail our investigations into the mechanism causing the shift in the $a^{\mathcal{E}}$ channel described in the main text. We identify the primary contribution to $a^{\mathcal{E}}$ as a light shift (AC Stark shift) that is differential between the two interferometer arms, a^{ls} . It differs between the two elevator positions ($\tilde{\mathcal{E}} = \pm 1$) and varies linearly with z owing to the divergence of the optical lattice mode.

Modelling the lattice laser beam as a Gaussian beam, its intensity varies as $I(z) = I_0[1 - (\lambda z)^2/(\pi w_0^2)^2]$, in which $w_0 = 760 \mu\text{m}$ is the waist and z is the position along the cavity axis with respect to the waist. At each vertical interferometer position, z , the difference between the intensity of the two interferometer arms is given by $\Delta I(z) = \partial I/\partial z \times \Delta z = -2I_0\lambda^2/(\pi w_0^2)^2 z \Delta z$.

Using equation (1), the measured acceleration is given by $a^{\text{ls}}(z) = \Delta U/(m_{\text{Cs}} \times \Delta z) = -2U_0\lambda^2/(\pi w_0^2)^2 z/m_{\text{Cs}}$.

This results in a differential acceleration shift during usual data-taking of $a^{\mathcal{E}} = (a^{\text{ls}}(z^{\mathcal{E}+}) - a^{\text{ls}}(z^{\mathcal{E}-}))/2$, in which $z^{\mathcal{E}\pm}$ are the vertical positions of the atoms at the two elevator positions.

To verify this model, we recorded an auxiliary dataset to measure $a^{\text{ls}}(z) - a^{\text{ls}}(0)$ at various z positions along the lattice axis in an auxiliary measurement (blue data points and fitted blue bands in Extended Data Fig. 3).

Because the above model unrealistically assumes atoms at zero temperature, we also estimate $a^{\text{ls}}(z)$ based on simulations of the trajectories of the atoms inside the optical lattice at the observed temperature of 300 nK, as described in ref. 10. Both the analytical model (dashed green line in Extended Data Fig. 3) and the simulation (dotted-dashed purple line in Extended Data Fig. 3) are found to be in good agreement with the slope extracted from the value of $a^{\mathcal{E}}$ for the entire dataset divided by the separation between the two elevator positions, $2(a^{\mathcal{E}})/(z^{\mathcal{E}+} - z^{\mathcal{E}-}) = -27 \text{ nm s}^{-2}/\text{mm}$ (solid red line in Extended Data Fig. 3). The model was further confirmed by our observation of a linear scaling of $a^{\mathcal{E}}$ with the trap depth U_0 .

Parameters varied in the search for systematic errors

Extended Data Tables 1 and 2 list parameters that were varied while searching for unexpected systematic errors. The procedure for performing these checks is described in the main text.

Prospects for investigating the inverse square law

Modifications to the Newtonian gravitational potential can be parametrized by a Yukawa-type potential correction with strength α and range λ

$$V(r) = -G_N(1 + \alpha e^{(-r/\lambda)}) m_1 m_2 / r.$$

To explore the sensitivity of our current experiment and future iterations to such new forces, we calculate their effect on the measured acceleration in our experiment, a_{mass} . We use a simple expression that includes the Yukawa term to compute the potential along the axis of the cylinder⁵⁶:

$$\begin{aligned} V^{\text{Yuk}}(z) = & (V^{\text{Newt}}(z, R_2, L) - V^{\text{Newt}}(z, R_1, L)) \\ & - 2\pi G\rho\alpha\lambda(I(z, R_2, L, \lambda) - I(z, R_1, L, \lambda)), \end{aligned}$$

in which R_2 , R_1 and L are the outer radius, inner radius and length of the cylinder,

$$I(z, R, L, \lambda) = \int_0^{L/2-z} e^{-\sqrt{s^2+R^2}/\lambda} ds + \int_0^{L/2+z} e^{-\sqrt{s^2+R^2}/\lambda} ds,$$

and the gravitational potential along the axis of a cylinder is

$$\begin{aligned} V^{\text{Newt}}(z, R, L) = & -\pi G\rho[(L/2-z)\sqrt{(L/2-z)^2+R^2} - (L/2-z)^2 \\ & + (L/2+z)\sqrt{(L/2+z)^2+R^2} - (L/2+z)^2]. \end{aligned}$$

Using these, we calculate the Newtonian acceleration, $a_{\text{mass}}^{\text{Newt}}(z) = c_1 \partial(V^{\text{Newt}}(z, R_2, L) - V^{\text{Newt}}(z, R_1, L))/\partial z$, and the acceleration that includes the Yukawa term, $a_{\text{mass}}^{\text{Yuk}}(z) = c_1 \partial V^{\text{Yuk}}(z)/\partial z$, for which the factor $c_1 = 0.85$ accounts for the missing mass from the rectangular slot in the hollow cylinder source mass.

We then calculate the cumulative distribution function of the value of $|\alpha|$ that leads to a 2σ deviation (corresponding to a 95% confidence interval) between the Newtonian value of acceleration, $a_{\text{mass}}^{\text{Newt}}$, and the value that includes the Yukawa term, $a_{\text{mass}}^{\text{Yuk}}$, for each value λ .

The resulting bounds are plotted in Fig. 4d, along with projections based on an experiment in which the atoms are held at a distance of 100 μm from a cavity mirror and measure deviations from the expected mirror Newtonian gravity. Several experiments have used atoms near a mirror for measurement^{17,57–59}, demonstrating the feasibility of this experimental geometry.

To explore whether diffuse scattering from the mirror could limit interferometer coherence, we ran simulations using the numerical framework described in a previous manuscript¹⁰. We quantify decoherence owing to the difference in scattered intensity between the two atom interferometer arms. The scattered light distribution is assumed to follow a Lambertian cosine law. We assume the worst-case scenario

Article

that the entire scattered intensity is concentrated at a single point. Extended Data Fig. 4 shows the resulting decoherence rate as a function of scattered intensity. Decoherence sets in when surface scatter is more than 100 ppm of the incident power. High-quality mirrors with scatter in the approximately 5 ppm range^{60,61} have been demonstrated, which is sufficient to avoid decoherence. Differentiating between the signal and surface effects, such as from Casimir forces, could be done using different internal atomic states⁶².

Data availability

All data presented in this paper are deposited online⁶³.

Code availability

Analysis code is available on request.

56. Hammad, F., Landry, A. & Mathieu, K. Prospects for testing the inverse-square law and gravitomagnetism using quantum interference. *Int. J. Mod. Phys. D* **30**, 2150004 (2020).
57. Harber, D. M., Obrecht, J. M., McGuirk, J. M. & Cornell, E. A. Measurement of the Casimir-Polder force through center-of-mass oscillations of a Bose-Einstein condensate. *Phys. Rev. A* **72**, 033610 (2005).
58. Sorrentino, F. et al. Quantum sensor for atom-surface interactions below 10 μm. *Phys. Rev. A* **79**, 013409 (2009).
59. Balland, Y., Absil, L. & Pereira dos Santos, F. Quesonewton local force sensor. Preprint at <https://arxiv.org/abs/2310.14717> (2023).
60. Billingsley, G., Yamamoto, H. & Zhang, L. Characterization of advanced LIGO core optics. *Am. Soc. Precis. Eng.* **66**, 78–83 (2017).
61. Turnbaugh, C. et al. High-power near-concentric Fabry-Perot cavity for phase contrast electron microscopy. *Rev. Sci. Instrum.* **92**, 053005 (2021).
62. Wolf, P. et al. From optical lattice clocks to the measurement of forces in the Casimir regime. *Phys. Rev. A* **75**, 063608 (2007).
63. Panda, C. D. et al. Measuring gravitational attraction with a lattice atom interferometer. Zenodo <https://doi.org/10.5281/zenodo.10995225> (2024).

Acknowledgements We thank A. Reynoso and J. Egelhoff for experimental assistance; J. Lopez, T. Gutierrez and G. Long for technical support; G. Louie and P. Bhattacharyya for discussions and comments on the manuscript; J. Axelrod, B. Elder, M. Jaffe, P. Haslinger, Y. Murakami, A. Singh and V. Xu and the entire Müller group for valuable discussions. This material is based on work supported by: National Science Foundation grants 1708160 and 2208029 (H.M.); Department of Defense Office of Naval Research grant N00014-20-1-2656 (H.M.); and Jet Propulsion Laboratory (JPL) grants 1659506 and 1669913 (H.M.).

Author contributions C.D.P., M.J.T. and M.C. built the apparatus and implemented experimental upgrades. C.D.P. designed the data-acquisition sequence and analysed data. C.D.P. and M.J.T. collected data. H.M. conceptualized and supervised the experiment. C.D.P. and H.M. wrote the original draft. J.K. and G.M.T. participated in the writing of the introduction and conclusion, highlighting the implications of the results for the fields of fundamental physics and atom interferometry. All authors contributed to the review and editing of the manuscript.

Competing interests The authors declare no competing interests.

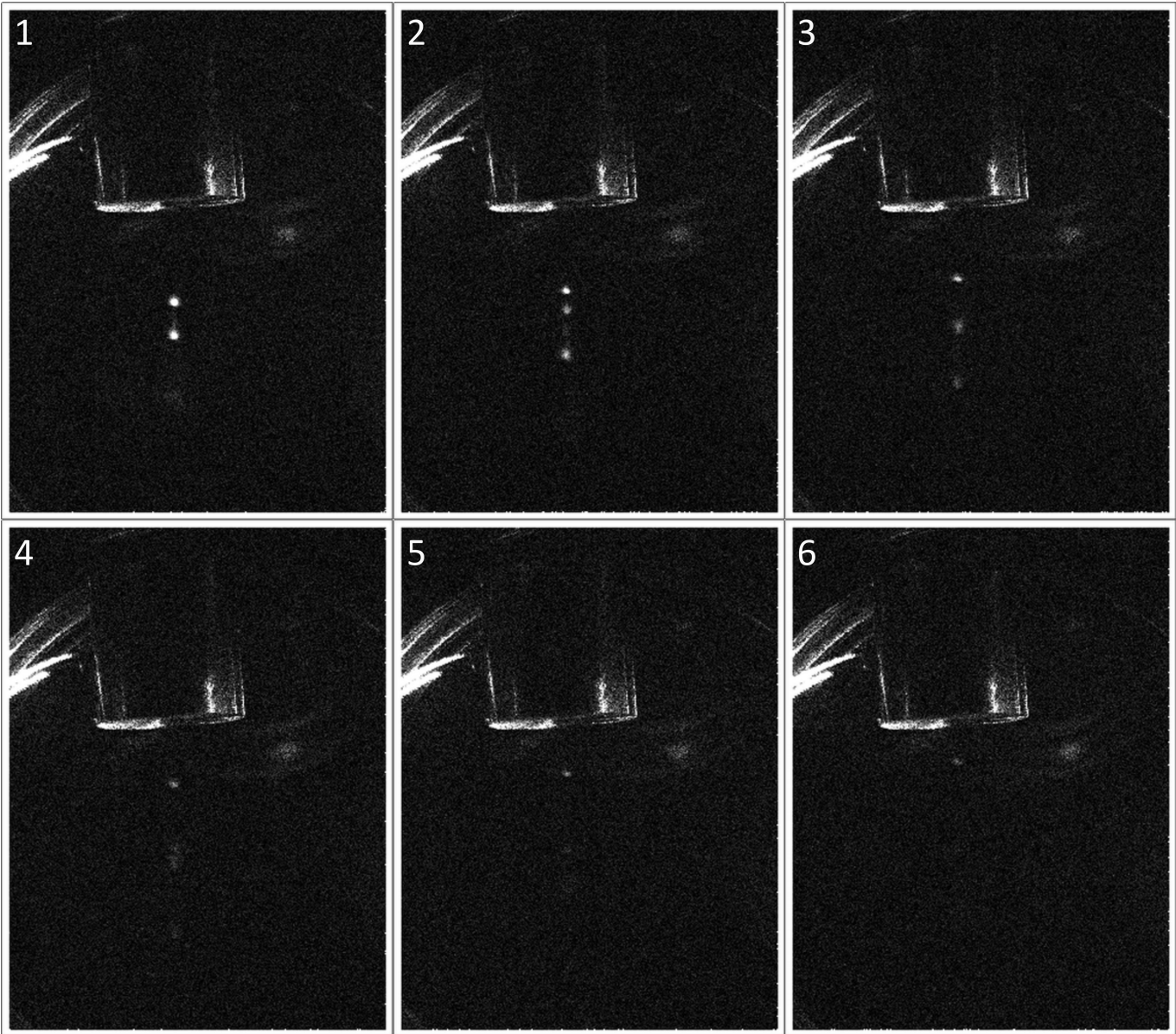
Additional information

Supplementary information The online version contains supplementary material available at <https://doi.org/10.1038/s41586-024-07561-3>.

Correspondence and requests for materials should be addressed to Cristian D. Panda or Holger Müller.

Peer review information *Nature* thanks the anonymous reviewers for their contribution to the peer review of this work. Peer reviewer reports are available.

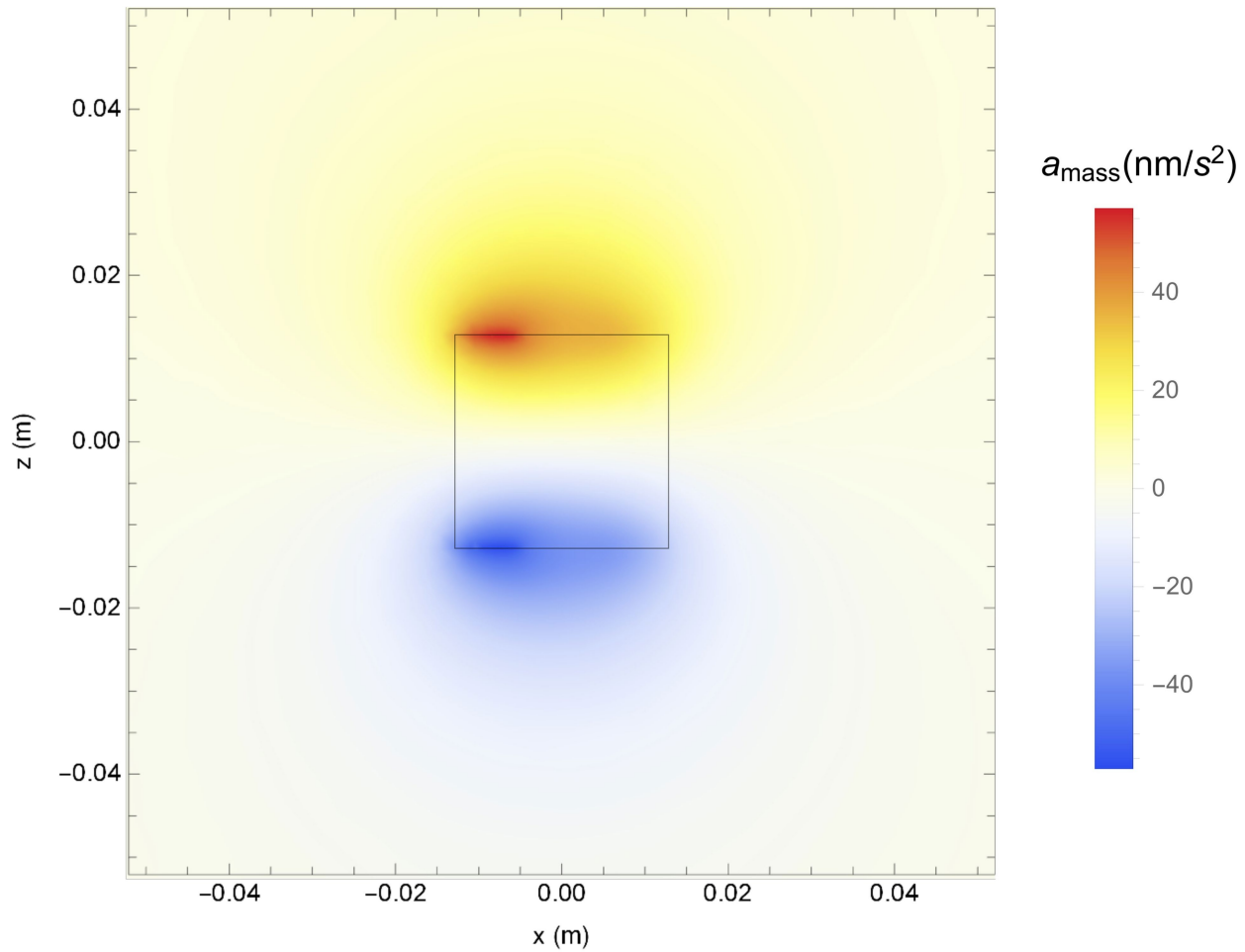
Reprints and permissions information is available at <http://www.nature.com/reprints>.



Extended Data Fig. 1 | Atom sample entering source mass. Sequence of images showing the Cs atom sample at various positions along its atomic elevator trajectory. Acquiring this sequence from three different perspectives

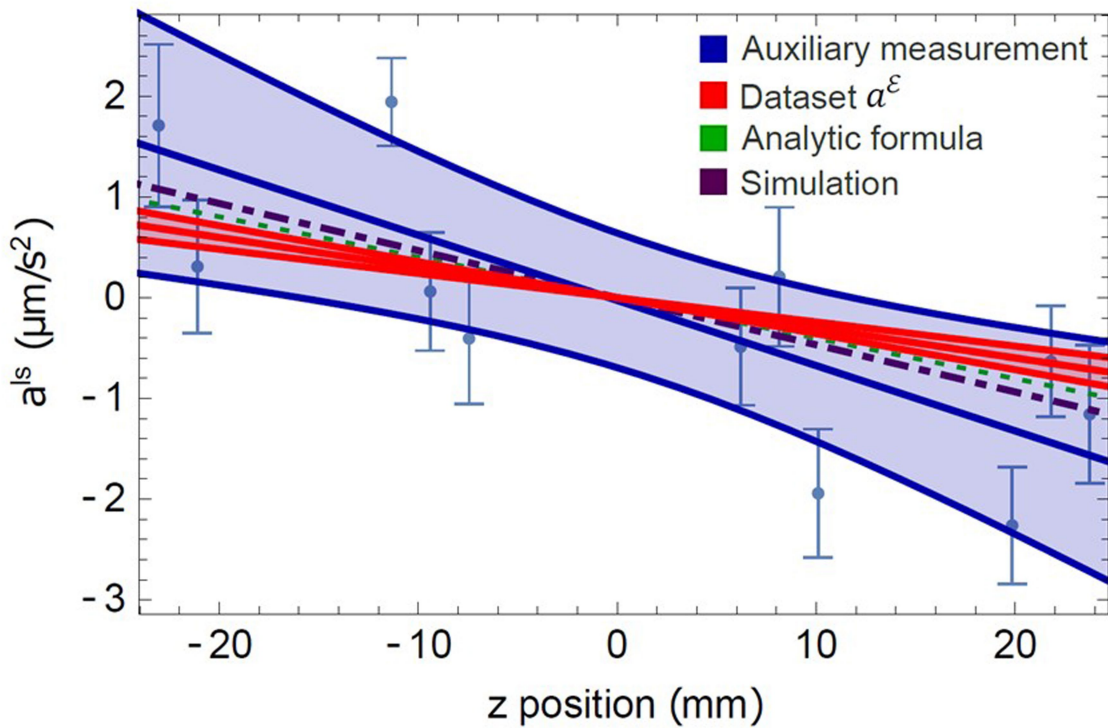
triangulates the position of the atom sample with respect to the source mass with an accuracy better than 1 mm.

Article



Extended Data Fig. 2 | Map of source-mass gravity. A 2D slice of the z component of the gravitational field calculated using finite element analysis in COMSOL is shown. The black square shows the extent of the hollow cylinder.

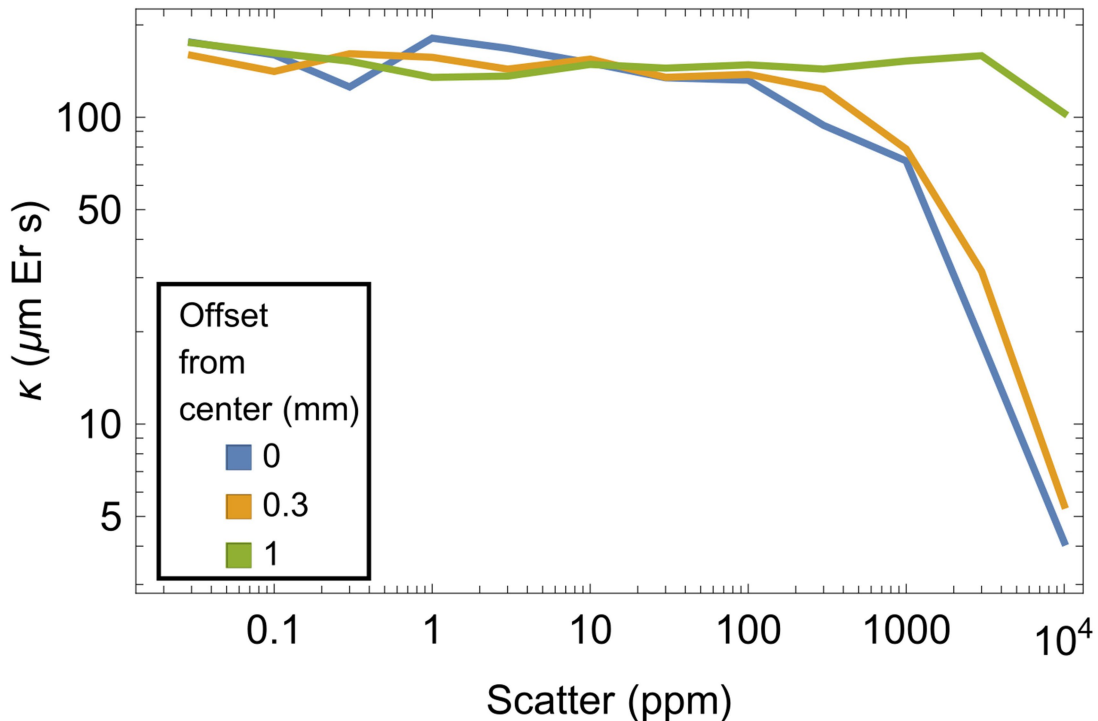
Gravity is stronger on the left side of the map because of the presence of the rectangular slot on the right side.



Extended Data Fig. 3 | Acceleration shift owing to lattice divergence a^{ls} .

In an auxiliary measurement, we observe a linear change in measured acceleration a^{ls} as a function of vertical position z . This is because of the differential AC Stark shift from the changing trap potential, $\Delta U(z)$, as the atoms

are held in various positions along the diverging lattice potential. We observe good agreement between the analytic equation derived above, simulation and experiment. The bands correspond to 95% (2σ) confidence intervals.



Extended Data Fig. 4 | Atom interferometer decoherence rate as a function of scatter. Projected lattice atom interferometer decoherence (contrast decay κ) versus level of scatter of the surface of the mirror. The atoms are held 100 μm

from the mirror at three different offset distances between the atom cloud and scatterer positions: 0, 0.3 and 1.0 mm. We observe marked decoherence when the scattered intensity is more than 100 ppm of the incident laser power.

Extended Data Table 1 | Parameters varied in the search for unexpected systematic errors

Category	Parameter Varied	Unit	Applied value(s) (unit)	Ambient variation, δP (unit)	Slope Mean, S_P (nm/s ² /unit)	Slope Uncertainty, δS_P (nm/s ² /unit)
Lattice parameters	Trap depth	arb unit	0.9, 1.2, 1.6	0.01	165	180
	Separation	μm	4.2, 6.6, 9.4	0.05	74	133
	Hold time	s	1.5, 2.2, 2.8, 3.6	10 ⁻⁶	0.0179	0.0581
	Lattice laser polarization ellipticity	%	0.40	1	-0.62	2.37
	Lattice laser frequency noise	arb unit	1,20	1	7.6	4.6
	Transverse temperature (via LG10 mode)	mK	0.3,0.16	0.001	690	1443
Beamsplitters	Raman laser detuning	kHz	-34,16	2	9.2	6.17
	Raman laser intensity all pulses	V	1.8,2.1,2.5	0.01	219	228
	Raman laser intensity one pulse	V	2.1,2.5,2.9	0.01	-154.5	290.9
	Beamsplitter height	ms	7,11,14	0.01	-26.3	17.2
Interferometer Environment	z B-field offset	V	-0.6, -0.25, 0.	0.002	91.8	450.2
	x B-field offset	V	-0.35, 0.0, 0.25	0.002	108	286
	y B-field offset	V	-0.5, -0.3, -0.1, 0.0, 0.1, 0.2, 0.6	0.002	-53.9	208
	MOT B-field applied during interferometer	mG/cm	15000	10	0.022	0.015
	Tracer intensity	mW	1,4	0.01	37.5	66.9
	Experiment tilt	V	3	0.05	13.8	32.4
Mass Correlated Parameters	Trap depth correlated with \tilde{M}		0.2,0.04	0.00032	340	914
	x MOT B-field correlated with \tilde{M}	V	0.5, 0.85	0.007	-57.9	259
	y Interferometer B-field correlated with \tilde{M}	V	0.3	0.002	206	413
	z Interferometer B-field correlated with \tilde{M}	V	0.3	0.002	-119	404

Parameters are categorized by the part of the experimental cycle to which they belong. Each parameter is varied over a range that is as large as possible, limited by decreases in signal size or contrast. Slope and uncertainty resulting from fitting the data to a linear slope are shown. RSC refers to Raman sideband cooling and PGC refers to polarization gradient cooling.

Article

Extended Data Table 2 | Parameters varied in the search for unexpected systematic errors—continued

Category	Parameter Varied	Unit	Applied value(s) (unit)	Ambient variation, δP (unit)	Slope Mean, S_p (nm/s ² /unit)	Slope Uncertainty, δS_p (nm/s ² /unit)
Sample prep - after launch	Velocity selection disabled		3	0.01	54.7	121.7
	Velocity selection duration	μs	130, 260	1.3	-1.04	0.7
	Velocity selection detuning	kHz	-22, 0, 6, 14	2	3.587	7.22
	Atom number (via microwave π -pulse duration)	μs	24, 44	3	-9.23	6.79
	Launch laser intensity	V	2,4,8	0.1	16.3	31.8
	Elevator laser intensity	V	2,4,6,10	0.1	-20.5	17.6
Sample prep - before launch	RSC duration	ms	2,4,40	0.001	1.24	2.95
	RSC 1D beam intensity	V	0.5, 1.1, 2	0.1	-411	485
	RSC 2D beam intensity	V	5, 6, 7, 8, 10	0.5	-43.5	37.5
	RSC pumping intensity	arb unit	1, 0.5	0.1	164	187
	PGC duration	ms	0, 10, 50	0.001	-21.2	18.9
	Hold time after sample prep	ms	1.8, 200, 500	0.001	0.055	0.4
Sample prep B-fields	MOT B-field x offset	V	-0.35, 0.0, 0.55	0.05	-196	304
	MOT B-field y offset	V	-0.2, 0.0, 0.2	0.05	410.2	427
	MOT B-field z offset	V	-0.8, -0.6, 0.0	0.05	-102	110
Imaging	Camera exposure time	ms	1, 2, 4	0.001	50.6	31.4
	Atom imaging position 2 mm higher	ms	10	0.1	-3.3	13.45
	Atom imaging position 1 mm higher	ms	5	0.1	-31	19
	Blowaway time	ms	14, 20	0.1	-1.97	8.67